

Human retinal imaging using visible-light optical coherence tomography guided by scanning laser ophthalmoscopy

Ji Yi,^{1,3} Siyu Chen,^{1,3} Xiao Shu,^{1,3} Amani A. Fawzi,² and Hao F. Zhang^{1,2,*}

¹Department of Biomedical Engineering, Northwestern University, 2145 Sheridan Rd., Evanston, IL, 60208 USA

²Department of Ophthalmology, Feinberg School of Medicine, Northwestern University, 645 N Michigan Ave, Chicago, IL 60611 USA

³These authors contributed equally to this work

*hfzhang@northwestern.edu

Abstract: We achieved human retinal imaging using visible-light optical coherence tomography (vis-OCT) guided by an integrated scanning laser ophthalmoscopy (SLO). We adapted a spectral domain OCT configuration and used a supercontinuum laser as the illuminating source. The center wavelength was 564 nm and the bandwidth was 115 nm, which provided a 0.97 μm axial resolution measured in air. We characterized the sensitivity to be 86 dB with 226 μW incidence power on the pupil. We also integrated an SLO that shared the same optical path of the vis-OCT sample arm for alignment purposes. We demonstrated the retinal imaging from both systems centered at the fovea and optic nerve head with $20^\circ \times 20^\circ$ and $10^\circ \times 10^\circ$ field of view. We observed similar anatomical structures in vis-OCT and NIR-OCT. The contrast appeared different from vis-OCT to NIR-OCT, including slightly weaker signal from intra-retinal layers, and increased visibility and contrast of anatomical layers in the outer retina.

©2015 Optical Society of America

OCIS codes: (110.4190) Multiple imaging; (170.0110) Imaging systems; (170.4470) Ophthalmology; (170.4500) Optical coherence tomography.

References and links

1. D. Huang, E. A. Swanson, C. P. Lin, J. S. Schuman, W. G. Stinson, W. Chang, M. R. Hee, T. Flotte, K. Gregory, C. A. Puliafito, and G. James, "Optical coherence tomography," *Science* **254**(5035), 1178–1181 (1991).
2. M. Wojtkowski, R. Leitgeb, A. Kowalczyk, T. Bajraszewski, and A. F. Fercher, "In vivo human retinal imaging by Fourier domain optical coherence tomography," *J. Biomed. Opt.* **7**(3), 457–463 (2002).
3. W. Drexler and J. G. Fujimoto, *Optical coherence tomography: technology and applications* (Springer Science & Business Media, 2008).
4. B. White, M. Pierce, N. Nassif, B. Cense, B. Park, G. Tearney, B. Bouma, T. Chen, and J. de Boer, "In vivo dynamic human retinal blood flow imaging using ultra-high-speed spectral domain optical coherence tomography," *Opt. Express* **11**(25), 3490–3497 (2003).
5. Y. Wang, B. A. Bower, J. A. Izatt, O. Tan, and D. Huang, "In vivo total retinal blood flow measurement by Fourier domain Doppler optical coherence tomography," *J. Biomed. Opt.* **12**(4), 041215–041218 (2007).
6. R. M. Werkmeister, N. Dragostinoff, S. Palkovits, R. Told, A. Boltz, R. A. Leitgeb, M. Gröschl, G. Garhöfer, and L. Schmetterer, "Measurement of absolute blood flow velocity and blood flow in the human retina by dual-beam bidirectional Doppler fourier-domain optical coherence tomography," *Invest. Ophthalmol. Vis. Sci.* **53**(10), 6062–6071 (2012).
7. B. Baumann, B. Potsaid, M. F. Kraus, J. J. Liu, D. Huang, J. Hornegger, A. E. Cable, J. S. Duker, and J. G. Fujimoto, "Total retinal blood flow measurement with ultrahigh speed swept source/Fourier domain OCT," *Biomed. Opt. Express* **2**(6), 1539–1552 (2011).
8. Y. Jia, S. T. Bailey, D. J. Wilson, O. Tan, M. L. Klein, C. J. Flaxel, B. Potsaid, J. J. Liu, C. D. Lu, M. F. Kraus, J. G. Fujimoto, and D. Huang, "Quantitative Optical Coherence Tomography Angiography of Choroidal Neovascularization in Age-Related Macular Degeneration," *Ophthalmology* **121**(7), 1435–1444 (2014).
9. S. Makita, F. Jaillon, M. Yamanari, M. Miura, and Y. Yasuno, "Comprehensive in vivo micro-vascular imaging of the human eye by dual-beam-scan Doppler optical coherence angiography," *Opt. Express* **19**(2), 1271–1283 (2011).
10. R. K. Wang, L. An, P. Francis, and D. J. Wilson, "Depth-resolved imaging of capillary networks in retina and choroid using ultrahigh sensitive optical microangiography," *Opt. Lett.* **35**(9), 1467–1469 (2010).

11. E. C. Lee, J. F. de Boer, M. Mujat, H. Lim, and S. H. Yun, "In vivo optical frequency domain imaging of human retina and choroid," *Opt. Express* **14**(10), 4403–4411 (2006).
12. Y. Yasuno, Y. Hong, S. Makita, M. Yamanari, M. Akiba, M. Miura, and T. Yatagai, "In vivo high-contrast imaging of deep posterior eye by 1- μ m swept source optical coherence tomography and scattering optical coherence angiography," *Opt. Express* **15**(10), 6121–6139 (2007).
13. R. Huber, D. C. Adler, V. J. Srinivasan, and J. G. Fujimoto, "Fourier domain mode locking at 1050 nm for ultra-high-speed optical coherence tomography of the human retina at 236,000 axial scans per second," *Opt. Lett.* **32**(14), 2049–2051 (2007).
14. J. P. Kolb, T. Klein, C. L. Kufner, W. Wieser, A. S. Neubauer, and R. Huber, "Ultra-widefield retinal MHz-OCT imaging with up to 100 degrees viewing angle," *Biomed. Opt. Express* **6**(5), 1534–1552 (2015).
15. J. P. Kolb, T. Klein, W. Wieser, W. Draxinger, and R. Huber, "Full volumetric video rate OCT of the posterior eye with up to 195.2 volumes/s," *SPIE BiOS. International Society for Optics and Photonics*, 931202–931207 (2015).
16. T. Klein, W. Wieser, C. M. Eigenwillig, B. R. Biedermann, and R. Huber, "Megahertz OCT for ultrawide-field retinal imaging with a 1050 nm Fourier domain mode-locked laser," *Opt. Express* **19**(4), 3044–3062 (2011).
17. T. Klein, W. Wieser, L. Reznicek, A. Neubauer, A. Kampik, and R. Huber, "Multi-MHz retinal OCT," *Biomed. Opt. Express* **4**(10), 1890–1908 (2013).
18. S. L. Jacques, "Optical properties of biological tissues: a review," *Phys. Med. Biol.* **58**(11), R37–R61 (2013).
19. J. Yi, Q. Wei, W. Liu, V. Backman, and H. F. Zhang, "Visible-light optical coherence tomography for retinal oximetry," *Opt. Lett.* **38**(11), 1796–1798 (2013).
20. F. E. Robles, C. Wilson, G. Grant, and A. Wax, "Molecular imaging true-colour spectroscopic optical coherence tomography," *Nat. Photonics* **5**(12), 744–747 (2011).
21. J. Yi and X. Li, "Estimation of oxygen saturation from erythrocytes by high-resolution spectroscopic optical coherence tomography," *Opt. Lett.* **35**(12), 2094–2096 (2010).
22. F. E. Robles, S. Chowdhury, and A. Wax, "Assessing hemoglobin concentration using spectroscopic optical coherence tomography for feasibility of tissue diagnostics," *Biomed. Opt. Express* **1**(1), 310–317 (2010).
23. J. Yi, W. Liu, S. Chen, V. Backman, N. Sheibani, C. M. Sorenson, A. Fawzi, R. Linsenmeier, and H. F. Zhang, "Visible light optical coherence tomography measures retinal oxygen metabolic response to systemic oxygenation," *Light Sci. Appl.* In press.
24. V. J. Srinivasan, S. Sakadzic, I. Gorczynska, S. Ruvinskaya, W. Wu, J. G. Fujimoto, and D. A. Boas, "Quantitative cerebral blood flow with optical coherence tomography," *Opt. Express* **18**(3), 2477–2494 (2010).
25. R. C. Gonzalez, R. E. Woods, and S. L. Eddins, *Digital image processing using MATLAB* (Pearson Education India, 2004).
26. B. Povazay, K. Bizheva, A. Unterhuber, B. Hermann, H. Sattmann, A. F. Fercher, W. Drexler, A. Apolonski, W. J. Wadsworth, J. C. Knight, P. S. J. Russell, M. Vetterlein, and E. Scherzer, "Submicrometer axial resolution optical coherence tomography," *Opt. Lett.* **27**(20), 1800–1802 (2002).
27. X. Zhang, J. Hu, R. W. Knighton, X.-R. Huang, C. A. Puliafito, and S. Jiao, "Dual-band spectral-domain optical coherence tomography for in vivo imaging the spectral contrasts of the retinal nerve fiber layer," *Opt. Express* **19**(20), 19653–19659 (2011).
28. S. P. Chong, C. W. Merkle, C. Leahy, H. Radhakrishnan, and V. J. Srinivasan, "Quantitative microvascular hemoglobin mapping using visible light spectroscopic Optical Coherence Tomography," *Biomed. Opt. Express* **6**(4), 1429–1450 (2015).
29. S. Chen, J. Yi, and H. F. Zhang, "Measuring oxygen saturation in retinal and choroidal circulations in rats using visible light optical coherence tomography angiography," *Biomed. Opt. Express* **6**(8), 2840–2853 (2015).
30. F. C. Delori, R. H. Webb, and D. H. Sliney; American National Standards Institute, "Maximum permissible exposures for ocular safety (ANSI 2000), with emphasis on ophthalmic devices," *J. Opt. Soc. Am. A* **24**(5), 1250–1265 (2007).
31. J. Kur, E. A. Newman, and T. Chan-Ling, "Cellular and physiological mechanisms underlying blood flow regulation in the retina and choroid in health and disease," *Prog. Retin. Eye Res.* **31**(5), 377–406 (2012).
32. P. Y. Teng, J. Wanek, N. P. Blair, and M. Shahidi, "Response of Inner Retinal Oxygen Extraction Fraction to Light Flicker Under Normoxia and Hypoxia in Rat," *Invest. Ophthalmol. Vis. Sci.* **55**(9), 6055–6058 (2014).
33. E. A. Newman, "Functional hyperemia and mechanisms of neurovascular coupling in the retinal vasculature," *J. Cereb. Blood Flow Metab.* **33**(11), 1685–1695 (2013).
34. C. E. Riva, E. Logean, B. L. Petrig, and B. Falsini, "Effect of dark adaptation on retinal blood flow," *Klin. Monatsbl. Augenheilkd.* **216**(5), 309–310 (2000).
35. R. D. Braun, R. A. Linsenmeier, and T. K. Goldstick, "Oxygen consumption in the inner and outer retina of the cat," *Invest. Ophthalmol. Vis. Sci.* **36**(3), 542–554 (1995).

1. Introduction

Optical coherence tomography (OCT) is a three-dimensional imaging technique that offers micrometer-level resolution and millimeter-level penetration [1, 2]. Over the past two decades, OCT has been applied to various biological research studies and clinical practices, including dermatology, cardiology, urology, dentistry, oncology, pulmonology, and most successfully, ophthalmology [3]. The clear ocular medium allows direct optical access to the posterior segment of the eye and enables OCT to image anatomical structures in explicit

detail. Functional OCT imaging of retinal blood flow [4–7] and label-free retinal microangiography [8–10] also have been developed to supplement the structural information.

To date, all the reported human retinal OCT systems have used invisible light sources centered above 800 nm. Within these near-infrared (NIR) spectral ranges, the reduced optical absorption of water, melanin, and blood allows for excellent penetration depth through the entire choroidal layer. Spectral domain or Fourier domain OCT (SD-OCT or FD-OCT) systems with ~840-nm center wavelength remains prevalent in clinical settings, partly due to their relatively simple implementation, low cost, and other historical reasons. Swept-source OCT (SS-OCT) centered at ~1,000 nm is also an emerging ophthalmic OCT configuration, first demonstrated in 2006 by Lee *et al* [11]. SS-OCT offers deeper penetration down to the sclera [12, 13]. In addition, the A-line rate can be dramatically increased up to more than 1 MHz [14–17].

Compared with the current NIR light OCTs, the use of visible-light OCT (vis-OCT) could offer several advantages. First, given the same bandwidth coverage, vis-OCT provides better axial resolution due to the shorter center wavelength. Second, vis-OCT has a stronger back-scattered signal under the same irradiance, as the optical-scattering cross-section in biological tissue is often inversely correlated with the wavelength [18]. Third, because the illumination wavelengths are within the sensing spectrum of the retina, there may be a more direct relationship between the structure and the function of the retina, particularly with photoreceptors. For example, the light-sensing pigment rhodopsin converts light into electric signals. This process also could change the back-scattered signals and may reflect, for example, local rhodopsin concentration variation. Lastly, the optical absorption of the two forms of hemoglobins in the visible light spectral range offers excellent contrast to quantify hemoglobin oxygen saturation (sO_2) through depth-resolved spectroscopic analysis in OCT [19–22]. Furthermore, combined with retinal blood flow measurements, vis-OCT can accurately measure the oxygen metabolism of the entire retinal circulation [23].

Here, we present human retinal imaging by vis-OCT guided by scanning laser ophthalmoscopy (SLO). The system is improved and translated from our previously reported rodent vis-OCT system [23]. A supercontinuum light source provides visible light illumination centered at 564 nm. The system sensitivity was measured to be ~86 dB with 226 μ W incident power on the pupil plane. The SLO subsystem was integrated with the vis-OCT to align the focus and navigate the vis-OCT. We demonstrate human retinal imaging around the macular region and optic nerve head (ONH) using both imaging modalities.

2. Methods and materials

2.1 Human vis-OCT system setup

Our vis-OCT adapted the SD-OCT configuration. We integrated the vis-OCT system with an SLO subsystem for better guidance. The two subsystems share the same light source but have separate detection schemes, as shown in Fig. 1(a).

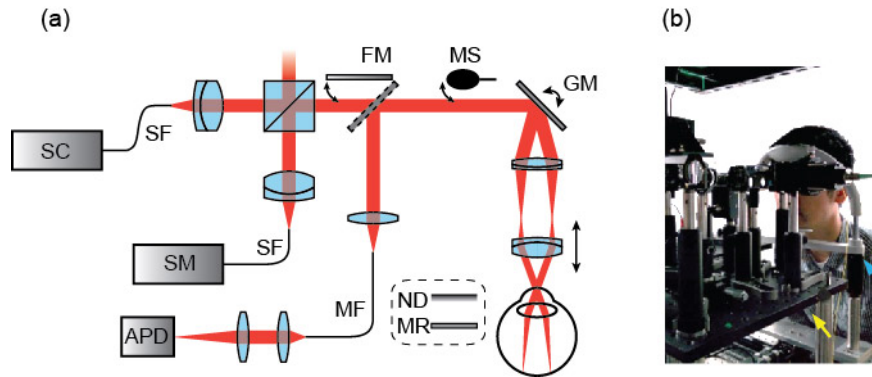


Fig. 1. (a) Schematic of the vis-OCT system for humans; (b) photograph of the system. SC: Supercontinuum laser source; SF: Single-mode fiber; SM: Spectrometer; Ref: Reference arm; FM: Motorized flip mirror; MS: Motorized beam stop; GM: Galvanometer mirror; MF: Multimode fiber; APD: Avalanche photodiode; MR: Mirror; ND: Neutral density filter. In (a), the ND and MR were placed at the position of eye ball to characterize the system performance. In (b), a blue arrow points to the three-dimensional translational chin rest for adjusting eye position; a yellow arrow points to the stationary optics board.

We used a supercontinuum laser (SuperK, NKT Photonics) as the vis-OCT light source. The wavelength range from 496 nm to 632 nm was selected by two edge filters (Semrock). The filtered light was coupled into a single-mode fiber (P3-460B-FC, Thorlabs), collimated, and delivered to a free-space Michaelson interferometer. A 70/30 beam splitter (BS019, Thorlabs) distributed 30% of the incoming energy to the sample arm and the remaining energy to the reference arm. In the sample arm, a pair of galvanometer mirrors (Nutfield Technology) raster-scanned the beam across a user-defined acquisition angle. The scanning pattern was projected onto the retina via a telecentric Keplerian telescope ($0.5 \times$ magnification), the ocular piece of which had an empirically chosen focal length of 35 mm. The ocular piece was mounted on a translational stage to adjust the focus on the retina. In the reference arm, we used a set of carefully chosen glass plates to compensate for the dispersion in the sample arm. A continuously adjustable reflective ND filter (NDC-50C-2M, Thorlabs) attenuated the beam intensity to enhance the dynamic range of the interference signal.

When the system was operated in the vis-OCT mode, the reflected beams from the sample and reference arms were recombined at the beam splitter, recoupled into a single-mode fiber, and delivered to a homemade spectrometer. The spectrometer consisted of an 1800-lpmm transmission grating (Wasatch Photonics) set at Littrow's angle optimized for a center wavelength of 564 nm. A line scan camera (spL2048-140km, Basler) digitized the dispersed spectrum at a speed of 25 kHz. The exposure time was 37 μ s, allowing 3 μ s for data readout. To ensure all the pixels are utilized, the spectrometer covered the spectral range from 506 nm to 621 nm, which is slightly narrower than the range after the laser passing through two edge pass filters from 496 nm to 632 nm.

When the system was operated in the SLO mode, a 50/50 beam splitter (FM in Fig. 1(a)) was flipped in the optical path of the sample arm. An achromatic lens focused the reflected sample beam onto the core of a multimode fiber (50 μ m core size, M16L01, Thorlabs). An avalanche photodetector (APD110A2, Thorlabs) detected the output light. The converted voltage signal from the APD was digitized by a multifunction acquisition card (PCI-6251, National Instruments) at 100 kHz sampling rate.

The entire optical system was mounted on a stationary optical breadboard. We used a chin rest mounted on a three-dimensional translation stage to position the eye, as shown in Fig. 1(b). We composed a LabVIEW (National Instruments) program for synchronization and data acquisition. Before and immediately after the acquisition, we programmed an electronic beam shutter to automatically block the light to avoid unnecessary exposure. As another protection mechanism, we parked the galvanometer mirrors at an angle so that the sample beam was reflected to a dumper after each imaging session.

2.2 Imaging acquisition

All the experimental procedures were approved by the Northwestern University Institutional Review Board and adhered to the tenets of the Declaration of Helsinki. Informed consent was obtained prior to imaging.

After a human subject placed his/her head securely and comfortably on the chin rest, we adjusted the head position so that the anterior surface of the eye was roughly at the focal plane of the ocular lens of the vis-OCT/SLO system. We took SLO fundus images first, as it is inherently faster and more suitable for alignment purposes. When operated in alignment mode, the SLO system generated fundus images at a pixel density of 256×64 and at a speed of 6 frames per second (fps). The real-time feedback allowed us to rapidly identify the region of interest (ROI) and optimize the axial focusing. After we identified the ROI and achieved satisfactory image quality, a high-density 512×512 SLO image was acquired, which took about 2.6 seconds. Both vis-OCT and SLO covered 10° or 20° field of view.

Once the SLO was aligned, we considered the vis-OCT to also be well aligned, since both systems shared the same illumination and optical path. After switching the system to vis-OCT mode, we scanned the same ROI and manually adjusted the position of the reference mirror. During axial alignment, low-density vis-OCT images (128×32 A-lines) were acquired and processed at 6 volumes per second (vps) continuously. Once the desired imaging quality was achieved, we recorded vis-OCT images at a higher density. Multiple scanning protocols were adopted. For general structural images, a 256×256 vis-OCT image stack took 2.6 seconds. When higher scanning density is required, a maximum of 262,144 A-lines can be achieved, which takes about 10.4 seconds. The maximum limit was set to avoid prolong imaging time which may cause eye discomfort or difficulty of fixation. The raster-scanning matrix could be arranged in the form of 512×512 , 2048×128 or 4096×64 , depending on the imaging requirement.

2.3 Data processing

We used MATLAB to process the acquired raw data. For the SLO signal, the recorded reflectance sequence was reshaped into an appropriate matrix to generate *en face* images. We performed histogram equalization to enhance the image contrast.

For vis-OCT, we followed conventional reconstruction algorithms in SD-OCT [24]. Briefly, we first estimated the background spectrum by averaging all A-line spectra in the same OCT image stack. The estimated background spectrum was subtracted from each A-line spectrum, and the resultant spectrum was further normalized by the background spectrum. For each individual A-line, we linearly resampled the normalized spectrum into equal wave number intervals (*k*-space). Finally, we performed Fourier transform on the interference signals and took the absolute values to generate cross-sectional and 3D anatomical images. We performed logarithm operations to enhance the dynamic range of the displayed images.

The axial eyeball motion was corrected after reconstructing the anatomical OCT images. We interpolated the images depth-wise by two folds, allowing correction of sub-pixel-size shifts. A cross-correlation was then performed along the *z*-direction between two adjacent B-scans. The peak locations of the calculated cross-correlation function was used to calculate the relative shifts. Then, each B-scan was shifted back to form registered images.

2.4 Human volunteers

All volunteers were informed about the inherent risks, had consented to the procedures prior to the imaging, and signed informed consent. Only one eye was imaged from each volunteer. When a large field of view (FOV) was required, we dilated the volunteer's pupil using 1% Tropicamide ophthalmic solution (Akorn), 30 minutes before imaging. For each volunteer, the whole procedure consisted of three to four sessions; each session included SLO and/or OCT imaging, as described above. The total time of a session was limited to five minutes, even if the images were not satisfactory. Volunteers were allowed to freely blink. Between two sessions, volunteers were allowed to rest for at least five minutes to recover.

After finishing all the imaging sessions, we asked the volunteers to rate the comfort of the procedure, and we monitored the subjects until their vision returned to normal, which usually took around five minutes or less. All the volunteers were evaluated using standard clinical retinal NIR-OCT and fundus auto-fluorescence (488nm and 787nm) imaging, and showed no sign of retinal damage.

We calculated the ANSI maximum permissible exposure (MPE) limit according to Eqs. (17-20) in [30] by Delori *et al.* These equations were originally laid out for SLO; since OCT has a similar scanning scheme, the equations should also apply to OCT. The current A-line rate is 25 kHz. To be most conservative, we chose the smallest FOV (10° square) and the highest scanning density (512×512) in our scanning protocols for the laser safety evaluation. The lowest MPE was calculated to be 3.6 mW for continuous exposure for two hours under CW limit (*i.e.*, a CW beam uniformly distributed over the entire field). Our illumination power on pupil was 226 μ W, which is more than ten times weaker than the MPE.

3. Results

3.1 System characterization

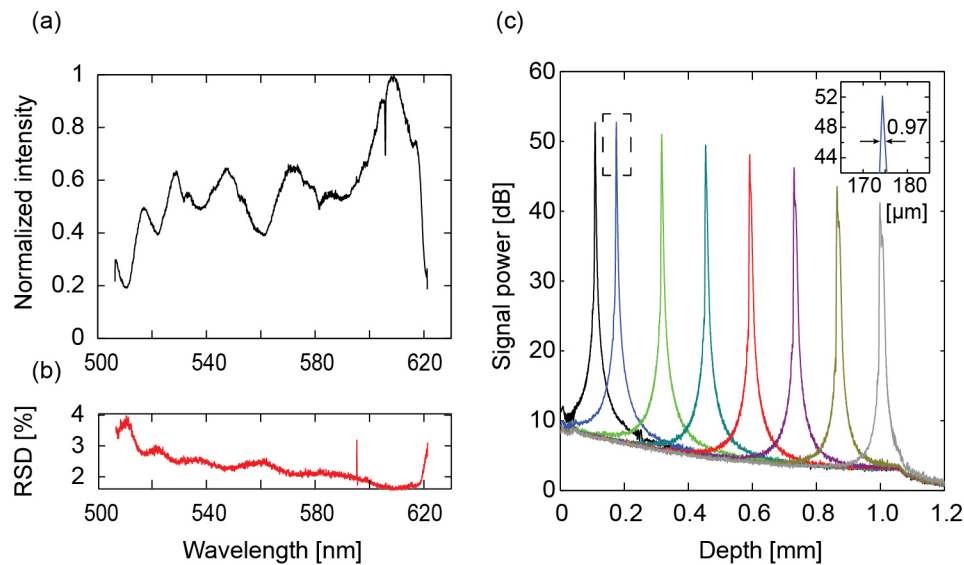


Fig. 2. System characterization. (a) Normalized spectrum measured by the spectrometer; (b) The relative standard deviation over 1,000 spectra acquired subsequently; (c) Measurements of axial resolution, system sensitivity, and sensitivity roll off.

First we characterized the performance of our vis-OCT system. Figure 2(a) shows the normalized light source spectrum captured by our homemade spectrometer. The spectrum covers 115 nm bandwidth centered at 564 nm. Figure 2(b) shows the wavelength-dependent stability of the light source, which was characterized by relative standard deviation (RSD) over 1,000 subsequent collections with 37 μ s exposure time. The RSD stayed within 3% for the central part of the spectrum. The power fluctuation from the supercontinuum laser produced a noise floor about 7-10 dB. Figure 2(c) illustrates the sensitivity of the system with respect to imaging depth. A silver mirror was placed behind the telescope to generate a sample signal by specular reflection. An ND filter (OD = 2.0) was placed in the optical path of the sample arm to introduce 40 dB attenuation. The illumination power on the mirror was measured to be 226 μ W (1918-R, Newport) and 2.2 μ W before and after placing the ND filter. The beam diameter was ~ 2 mm on the cornea. As shown in Fig. 2(c), the signal power is above 50 dB with a background noise floor of 7 dB. Because we usually place the image within 0.5 mm, the system sensitivity is estimated to be 86 dB. A roll-off effect is

characterized to be 12 dB/mm, because the spatial dimension of the pixel element in the spectrometer introduces an averaging effect that smoothes out the high-frequency interference. We also characterized the system axial resolution by the full-width-half-maximum value (−6 dB reduction from 52 dB to 46 dB) from the image of a silver mirror as the inset in Fig. 2(c). The experimentally measured axial resolution was 0.97 μm in air.

3.2 *In vivo* images of human retina by vis-OCT

A healthy volunteer (OD, + 3.0 Diopter) was imaged with our vis-OCT/SLO system. All the images were post-processed by median filtering and histogram specification to remove noise and maximize contrast [25]. Figure 3 shows the imaging result at the macular region. Figure 3(a), 3(b) are *en face* SLO and vis-OCT images, respectively. All the original images from Figs. 3(a)-3(d) consisted of 512×512 pixels. In the SLO image, the fovea appears as the central dark area, which is surrounded by hyper-reflectance of the macula. In both SLO and OCT images, specular reflection can be visualized in the center of the large blood vessels. We also took images on $10^\circ \times 10^\circ$ field of view centered at the fovea. To better visualize the finer vascular details, we cropped out the center $5^\circ \times 5^\circ$ field of view as shown in Figs. 3(c) and 3(d). The original images with $10^\circ \times 10^\circ$ field of view were attached as Appendix 1. In both SLO and vis-OCT images, retinal capillaries surrounding the fovea can be visualized. Figure 3(e) is a single B-scan consisting of 2048 A-lines taken from the location highlighted by the dashed line in Fig. 3(b). A total of 12 retinal layers can be recognized from the cross-section. The nerve fiber layer (NFL) on the temporal side of the fovea appears thicker than the nasal side. The inner retina shows weak scattering compared with the outer retina and the retinal pigment epithelium (RPE).

Within the retina, relatively higher signal intensity is generated by the NFL, inner-plexiform layer (IPL), and outer-plexiform layer (OPL). The layers containing cell nuclei, including ganglion cell layer (GCL), inner nuclear layer (INL), and outer nuclear layer (ONL) have lower signal. In the outer retina, the boundary between the photoreceptor inner and outer segment (IS/OS), the outer segment of photoreceptors (OS), and the RPE show similar back-scattering power. Due to the submicron depth resolution, the Bruch's membrane (BM) can be distinctly resolved. Little light penetrates through the RPE to the choroid due to the strong absorption of visible light by the RPE. We compared vis-OCT images with a commercially available NIR OCT system (Cirrus-HD-OCT, Carl Zeiss Meditec, Pleasanton, CA) from the same volunteer. The IS/OS, OS, and RPE layers appeared to have a higher contrast compared with the inner retinal layers in vis-OCT and compared with their corresponding outer retinal structures in NIR OCT (Fig. 3(e)). The zoomed-in details at RPE/BM in Fig. 3(e) and 3(f) were attached as Appendix 2. Figure 3(f) shows the averaged result of eight B-scans from the same location. Compared with the non-averaged B-scan (Fig. 3(f)), the noise is suppressed while some of the high spatial frequency features are smoothed out in the averaged image.

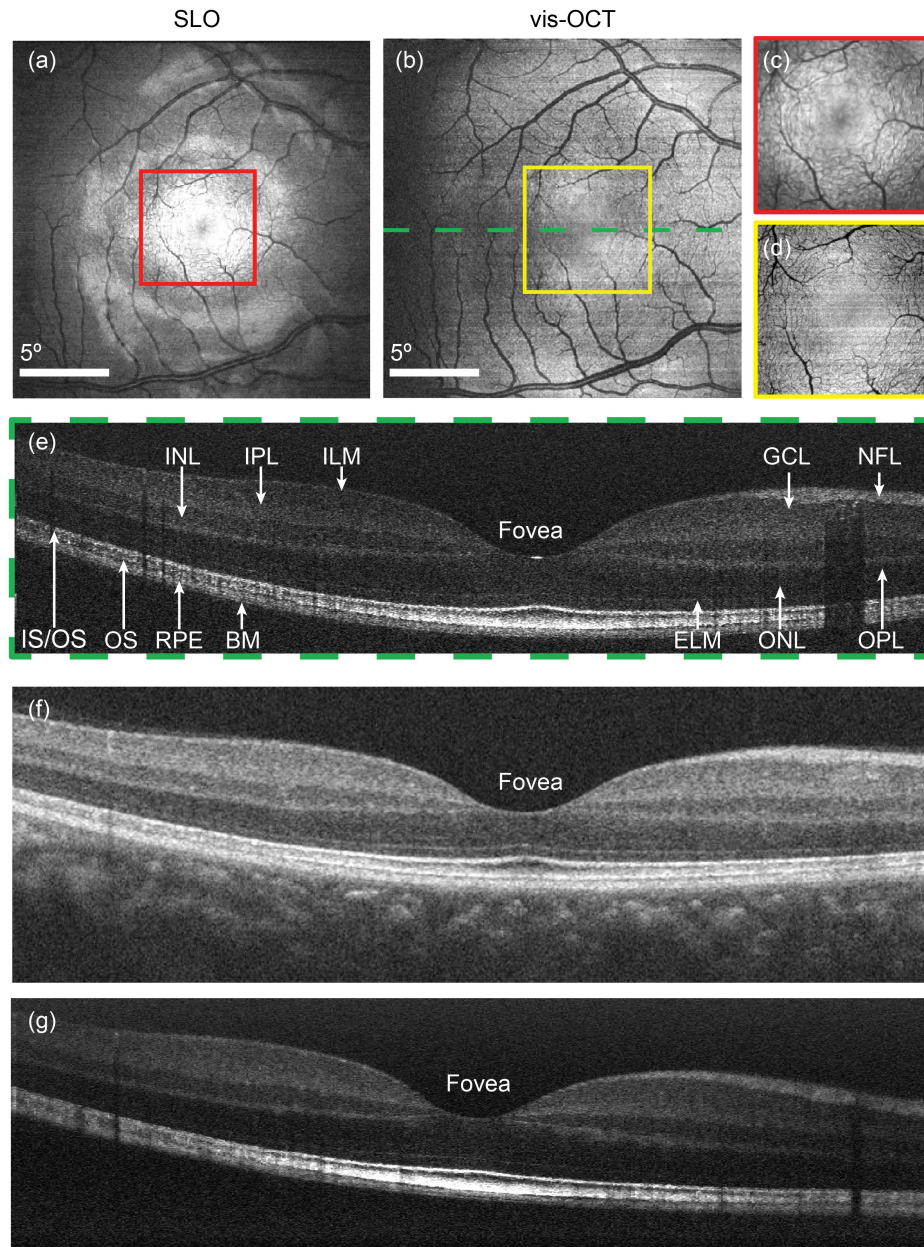


Fig. 3. SLO and vis-OCT images centered at the fovea. (a-b) En face images of SLO and vis-OCT; (c-d) Contrast-adjusted images from the squared area in (a) and (b); (e) Cross-sectional vis-OCT image from the position highlighted in (b) with all anatomical structures labeled. ILM: Inner-limiting membrane; NFL: Neural fiber layer; GCL: Ganglion cell layer; IPL: Inner plexiform layer; INL: Inner nuclear layer; OPL: Outer plexiform layer; ONL: Outer nuclear layer; IS/OS: Inner/outer segment junction; OS: Outer segment of photoreceptor; RPE: Retinal pigmented epithelium; BM: Bruch's membrane. (f) Single cross-sectional image using a commercial NIR-OCT system. (g) Averaged vis-OCT image from eight consecutive B-scans. The motion artifact was removed by aligning the adjacent B-scans.

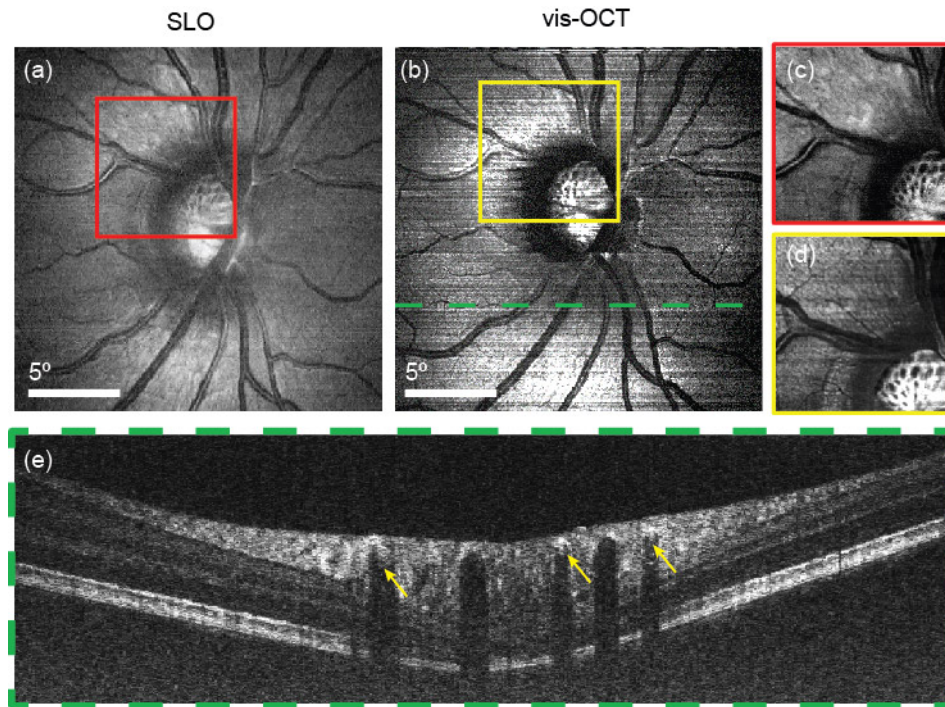


Fig. 4. SLO and vis-OCT images centered at ONH. (a-b) En face images from SLO and vis-OCT; (c-d) Contrast-adjusted images from the squared area in (a) and (b); (e) Cross-sectional vis-OCT image from the location highlighted in (b); Arrows points to the signal from blood within major retinal vessels.

Figure 4 shows the imaging result around ONH from the same volunteer. Figure 4(a) and 4(b) are *en face* images from SLO and vis-OCT (512×512 pixels). We also took scans within the squared area to better visualize the structural details. The optical focus of the temporal side of optic disk is moderately affected by the curvature of posterior eye. The fine features in the lamina cribrosa are observed on both imaging modalities. The texture of the nerve fibers can be clearly visualized on vis-OCT. Figure 4(e) shows the B-scan consisting of 2048 A-lines extracted from the dashed line shown in Fig. 4(b). The normally increased thickness of NFL close to ONH is obvious. Strong absorption in the major retinal blood vessels and most of the smaller vessels creates shadows beneath them. Scattering from blood within the vessels also can be observed.

The exquisite axial resolution is further demonstrated in Fig. 5. In the outer retina, the details of IS/OS, OS interdigitation zone, RPE, and BM are clearly distinguishable (Fig. 5(a)). Although the RPE melanin attenuates the visible light significantly, we can still obtain a signal from the choroid, which lies immediately beneath BM (Fig. 5(b)). In the NFL, the fine details of the structural texture can be visualized (Fig. 5(c)). The clear visualization of the outer retina may be attributed to the sub-micron axial resolution, and perhaps a better contrast between anatomical layers imaged by vis-OCT. Because retina is naturally designed to capture light within the visible-light spectral range, the commonly-believed increased light scattering due to short optical wavelength did not appear to degrade the resolution as can be observed in Fig. 5(b).

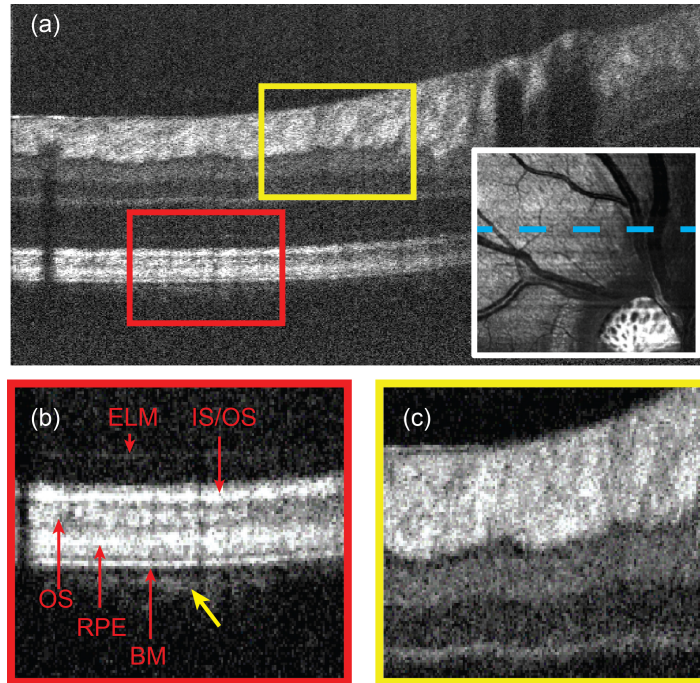


Fig. 5. (a) Cross-sectional vis-OCT image around ONH. The inset at the bottom-right corner shows the en face vis-OCT image where the B-scan is taken from. (b-c) Magnified images from the squared areas in (a). Arrow points to the signal from the choriocapillaris immediately beneath Bruch's membrane. The anatomical structures in the outer retina are labeled in (b).

4. Discussion and conclusion

In this work, we demonstrated the first human retinal imaging using vis-OCT guided by an integrated SLO. We characterized the detection sensitivity of vis-OCT to be 86 dB with 226 μ W illumination power on the pupil plane, and the axial resolution to be 0.97 μ m measured in air. SLO was integrated by sharing the optical path in the sample arm for alignment purposes. Retinal images from a healthy volunteer were demonstrated with $20^\circ \times 20^\circ$ and $10^\circ \times 10^\circ$ FOV centered at both the fovea and optic nerve head. The anatomical features in vis-OCT were similar to NIR-OCT. Because human retina senses and reacts to visible light, the interlayer contrast in vis-OCT can be expected to be different from NIR-OCT. For example, we observed slightly less contrast from INL, IPL, ONL and OPL; and better separation of layers in outer segment of photoreceptors and BM. Thus, the existing segmentation methods of retinal layers may need to be modified for vis-OCT. Nonetheless, the explicit details of the anatomical structures by vis-OCT may be a beneficial supplement to existing clinical NIR-OCT.

The first demonstration of using supercontinuum light for vis-OCT was reported using a sub-10-fs Ti:sapphire laser to pump a photonic crystal fiber covering from 550 nm to 950 nm [26]. The system was built upon a time domain configuration (TD-OCT) with a free-space interferometry. Because of the speed limit of TD-OCT, *in vivo* vis-OCT system on retina was not reported until a SD-OCT configuration was adopted [27]. In this first SD-vis-OCT system, the visible light was generated by focusing a Ti: Sapphire laser through a frequency doubling crystal. The advantage of using frequency doubling crystal over supercontinuum light was the better power stability. However, the bandwidth was only ~ 10 nm which limited the axial resolution. Because of the limited bandwidth, a fiber-based interferometry was used where dispersion within the fiber was less influential. The most recent implementations of retinal vis-OCT were based on an advanced supercontinuum laser source with a free-space interferometry in SD-OCT configuration [19, 28, 29], including our previous system on

rodents and the human vis-OCT system being reported here. The supercontinuum light provided a broad bandwidth for submicron axial resolution, while the free-space interferometry minimized the dispersion. Because the free-space interferometry requires precise alignment and mechanical stability, in our presented system, we mounted all the optical components on a stationary breadboard and moved the subject's head by a translational chinrest. Another technical improvement in this system is the integration of SLO, which provided real-time fundus image as a guidance to facilitate optical adjustment.

A major concern for the application of vis-OCT in human retinal imaging is laser safety. In this study, the incident power on the pupil was controlled at 226 μW , more than ten times less than the laser safety level calculated for continuous exposure for two hours [30]. There are also several mechanisms designed to prevent excessive exposure: we installed a motorized beam shutter, which only allows the beam to pass when the imaging session is on; when the imaging session is off, the galvanometer mirrors deflect any possible beam to a dumper.

There are also several practical considerations when applying vis-OCT in clinical settings. One question is whether the visible laser beam will affect retinal physiology, particularly when using vis-OCT to perform quantitative measurements such as blood flow and sO_2 . It has been found that both flow and retinal metabolism change when the retina transitions from dark adaptation to light or under flicker stimulation [31–33]; however, we do not expect such changes to occur when the retina has already been light-adapted [34, 35]. The additional exposure from vis-OCT is unlikely to change the physiological condition of the eye, thereby underscoring the importance of ensuring the patient's eye is light-adapted before vis-OCT imaging. The other practical concern is the distracting nature of the scanned visible-light OCT beam when the eye is focused on the fixation target. Currently, we used the fellow eye for fixation because the two eyes shared the same focus. Although it did not affect the data acquisition for multiple B-scans at a same location, it could be challenging to image a large field of view centered at the fovea, especially in patients with less stable fixation. Another solution is to integrate an invisible OCT channel for alignment purposes, with the vis-OCT channel turned on only at the time of data acquisition.

In summary we have demonstrated the feasibility and safety of the vis-OCT system in human retinal imaging. Further refinements of the technology and addressing the remaining technical issues are underway. We have shown the distinct differences between vis-OCT and NIR OCT, such as increased visibility of the outer retinal structures, including a distinctly visible BM, and increased scattering within the blood vessels and denser shadows beneath them. These differences will be harnessed in vis-OCT to improve our understanding of the pathophysiology of the various retinal layers in health and diseases.

Appendix 1:

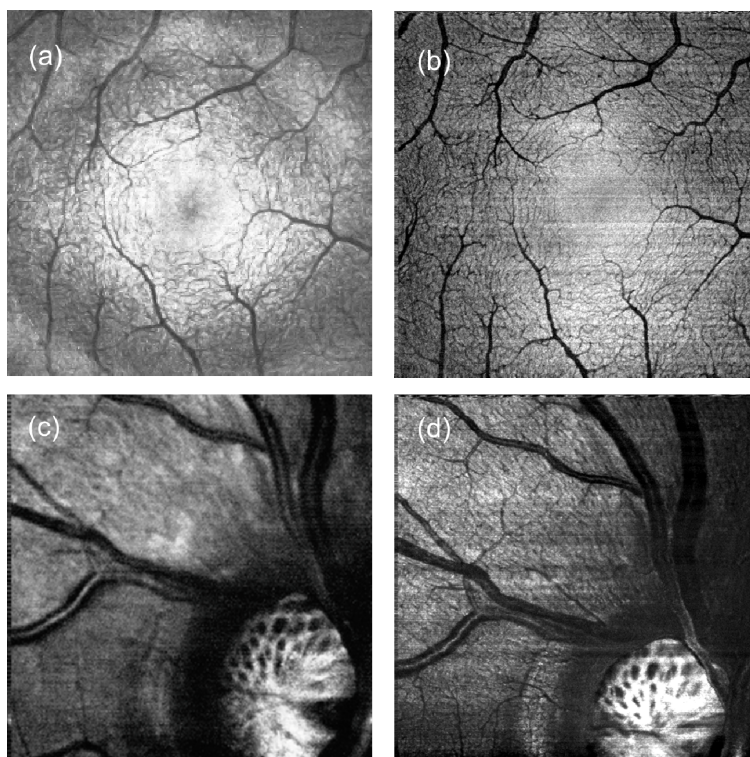


Fig. 6. Original $10^\circ \times 10^\circ$ field of view images. (a-d) original images for Fig. 3(c), 3(d) and Fig. 4(c), 4(d).

Appendix 2:

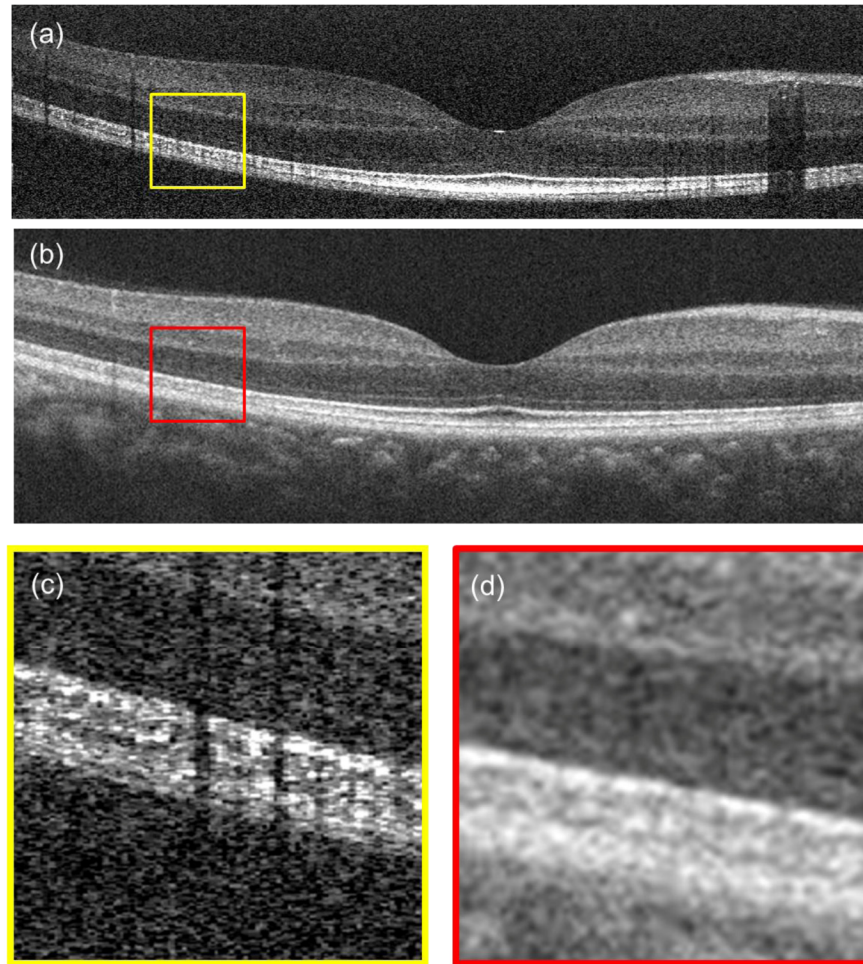


Fig. 7. Magnified images of RPE/BM structures from vis-OCT and NIR OCT. (a-b) Replots of Fig. 3(e) and 3(f). (c-d) 4x magnified images from the squared areas in (a) and (b).

Acknowledgments

We acknowledge the generous funding support from the National Institutes of Health (1R01EY019951 and 1R24EY022883) and the National Science Foundation (CBET-1055379, CBET-1066776, and DBI-1353952). J. Yi is supported in part by a postdoctoral fellowship award from the Juvenile Diabetes Research Foundation. H. F. Zhang has financial interests in Opticent Health Inc., which, however, did not support this work.